Soft Matter

rsc.li/soft-matter-journal

ROYAL SOCIETY
OF **CHEMISTRY**

PAPER
Jan Vermant *et al.*
Variations in human saliva viscoelasticity affect
aerosolization propensity

Check for updates

Variations in human saliva viscoelasticity affect aerosolization propensity†

Mariana Rodríguez-Hakim, [ID] Linard Räz and Jan Vermant [ID] *

Some contagious diseases, such as COVID-19, spread through the transmission of aerosols and droplets. Aerosol and droplet formation occurs inside and outside of the respiratory tract, the latter being observed during speaking and sneezing. Upon sneezing, saliva is expelled as a flat sheet, which destabilizes into filaments that subsequently break up into droplets. The presence of macromolecules (such as mucins) in saliva influences the dynamics of aerosol generation, since elasticity is expected to stabilize both fluid sheets and filaments, hence deterring droplet formation. In this study, the process of aerosol formation outside the respiratory tract is systematically replicated using an impinging jet setup, where two liquid jets collide and form a thin fluid sheet that can fragment into ligaments and droplets. The experimental setup enables us to investigate a range of dynamic conditions, quantified by the relevant non-dimensional numbers, which encompass those experienced during sneezing. Experiments are conducted with human saliva provided by different donors, revealing significant variations in their stability and breakup. We quantify the effect of viscoelasticity *via* shear and extensional rheology experiments, concluding that the extensional relaxation time is the most adequate measure of a saliva's elasticity. We summarize our results in terms of the dimensionless Weber, Reynolds, and Deborah numbers and construct universal state diagrams that directly compare our data to human sneezing, concluding that the aerosolization propensity is correlated with diminished saliva elasticities, higher emission velocities, and larger ejecta volumes. This could entail variations in disease transmission between individuals which hitherto have not been recognized.

1 Introduction

Aerosols and droplets that are produced upon sneezing, coughing, or speaking can lead to the transmission of contagious diseases such as COVID-19, influenza, and tuberculosis.[1–9] This airborne transmission process is governed by complex transport phenomena that span multiple length scales and geometries which determine, for instance, the boundary conditions that give rise to fluid flow. Aerosols and droplets are formed in various locations within the respiratory tract, such as the bronchioles and the larynx,[8,10,11] and continue to form and fragment at the exit of the nose and mouth.[4–6]

In particular, sneezing and speaking induce salivary fragmentation processes that occur outside of the respiratory tract.[5,6,12] Scharfman *et al.* use high speed videography of human subjects to directly observe the physical mechanism of aerosol and droplet formation during sneezing, revealing that their generation follows a complex sequence of events,

whereby the expelled mucus volume is flattened into a sheet that expands and thins over time due to the inertia of the surrounding air.[5] This is accompanied by the appearance of holes and thin filaments within the sheet, which subsequently destabilize and break up into aerosols and droplets.[5] This film-to-filament and filament-to-droplet transition is similarly documented by Abkarian and Stone, who report the formation of thin salivary films at the lips that destabilize into filaments and drops upon the pronunciation of plosive sounds.[6] However, the role of variations in saliva viscoelasticity on these phenomena have not been reported to date.

The resulting aerosols and droplets have radii on the order of microns to hundreds of microns, and depending on their size can either immediately sediment to the ground (droplets) or remain suspended in the air for hours (aerosols).[8,13] Although a distinction between aerosols and droplets is commonly made in the literature,[8,13] in this manuscript the terms aerosol and droplet are used interchangeably, and aerosolization is defined as the process by which they are formed.

The competition between inertial, capillary, viscous, and elastic stresses determines the morphology, stability, and breakup of the salivary sheets. The relative importance of these four forces is expressed in terms of three dimensionless groups:

Department of Materials, ETH Zürich, Vladimir-Prelog-Weg 5, Zürich, 8093, Switzerland. E-mail: jan.vermant@mat.ethz.ch; Tel: + 41 44 633 33 55

the Reynolds number (Re), the Weber number (We), and the Deborah number (De). The Reynolds number represents a competition between viscous and inertial stresses, and reflects the dominant force that drives the flow of salivary sheets. The Weber number quantifies the ratio between inertial forces, which drive sheet expansion and thinning, and capillary forces, which limit the radial expansion of the sheet.[14] Saliva ligaments can break up into droplets by virtue of the Rayleigh–Plateau instability, where surface tension drives the creation of spherical drops; thus, the Weber number also reflects the competition between the convective timescale that drives fluid flow and the capillary timescale that governs ligament destabilization. The Deborah number, defined as the ratio of the polymer's relaxation time divided by the capillary timescale, provides information on how the elasticity of the solution affects momentum transport and the stability of sheets and ligaments.

Since saliva is an elastic fluid, the instabilities that give rise to aerosols and droplets are strongly affected by its chemical makeup and mechanical properties. Less than 1% of the total salivary mass is composed of macromolecules such as mucins, DNA, and other proteins.[15,16] Mucins, which are high molecular weight glycosylated proteins, are responsible for providing the major physical and dynamical properties of mucus.[15,17,18] At the concentrations present in saliva, mucins exist in the semidilute unentangled regime and exhibit a complex viscoelastic network structure formed *via* hydrophobic and carbohydrate–carbohydrate interactions, calcium-mediated cross links, and hydrogen and disulfide bonds.[17–21] The viscoelastic character of the mucins has a strong effect on the generation of aerosols, since enhanced elasticity stabilizes thin fluid filaments and retards the onset of droplet formation by inducing tensile stresses that are incapable of fully relaxing back to equilibrium during filament stretching.[5,6,9,22,23]

The purpose of the present work is to quantify the effect of different dynamic conditions, such as the saliva's elasticity, the expiration velocity during sneezing, and the ejected saliva volume, on the generation of aerosols and droplets outside of the respiratory tract. Specifically, it is aimed at obtaining a more complete and quantitative understanding of the influence of salivary viscoelasticity on aerosolization, which has hitherto been understudied despite its fundamental influence in governing aerosolization processes. We also measure the material properties of saliva from different individuals, such as the elasticity, viscosity, and surface tension, and explore the extent to which variations in these parameters can account for disparities in disease transmission among the human population.

The aerosol and droplet formation process occurring outside of the respiratory tract is replicated and the relevant parameter space is systematically explored using an impinging jet setup, whereby the collision of two liquid jets forms a thin fluid sheet that can subsequently fragment into ligaments and droplets.[24,25] In this setup, sheet formation, expansion, and thinning occur due to the inertia of the incoming jets, as the momentum transferred by the two streams results in the formation of a flat sheet in the plane perpendicular to the plane of the jets.[24–26] Thus, although the mechanism driving sheet formation in our impinging jet experiments is different from the one giving rise to the freely-suspended sheets seen in sneeze events (these form due to the inertia of the surrounding air, which establishes an aerodynamic pressure gradient[5,14,27,28]), both scenarios exhibit the same inertia-driven morphology and dynamics that gives rise to sheet expansion and thinning. Furthermore, in both configurations, the balance between inertia and capillarity gives rise to a thicker cylindrical rim that bounds the edge of the sheets. Depending on the balance between elastic, convective, and capillary forces, these rims can destabilize into ligaments, which can subsequently disintegrate into droplets.

Even though the kinematics and stability of viscoelastic filaments is well understood,[22,23,29] non-Newtonian sheet expansion and deformation processes are more intricate and warrant further study, particularly to understand how the interplay between elasticity, inertia, and capillarity affects sheet stability and breakup. Thus, the impinging jet setup enables us to systematically study the deformation processes occurring within the thin saliva films produced upon sneezing and to understand how the viscoelastic stresses in saliva influence the shape of the sheet and the formation of the rim, leading up to aerosol-producing instabilities.

Impinging jet setups have been extensively used to characterize the behavior of Newtonian solutions, revealing a rich phase behavior that is attained as We and Re are independently varied.[24,25,30–32] A handful of works have investigated viscoelastic sheet formation, where now De controls the sheet dynamics and stability along with We and Re.[32–35] These works have revealed that fluid elasticity (1) delays the onset of sheet breakup,[34] (2) changes the morphology of the instabilities, and (3) broadens the size distribution of the resulting aerosols.[33,34] Thus, it is expected that polymeric mucins and other salivary macromolecules dramatically impact the aerosolization process when saliva is violently expelled from the mouth.

Experiments are conducted using human saliva provided by five different anonymous donors. Fresh human saliva samples were selected for experimentation over laboratory-prepared solutions of reconstituted commercial mucins of known concentration due to the inability of the reconstituted mucins to display the dynamical and rheological properties of native saliva.[18,19,36] Despite the fact that several studies that assess the influence of elasticity on the aerosolization of artificial mucus solutions have been conducted, the range of mucin concentrations, the types of intermolecular interactions, and the signature rheological properties of reconstituted mucins *vs.* native saliva are remarkably different.[18,19,36–38] Furthermore, a systematic understanding of the parameters affecting the aerosolization of native saliva during expiratory events and their variations among different individuals is still lacking, as experiments with human subjects offer little control over parameters such as expiration velocity and flow rate,[5,6,39,40] and numerical simulations have so far been limited to studying Newtonian solutions, where the effect of fluid elasticity is not taken into account.[41–44]

In our experiments, the dimensionless We, Re, and De are independently tuned by modulating the jet radius and flow rate in the impinging jet setup. The range of velocities and length scales is selected to match physiological conditions and our

experimental results are directly compared to human sneezing as reported in the literature.[5,39,40] We construct universal state diagrams that summarize the stability and aerosolizing behavior of the saliva from all donors. When directly comparing our experiments with documented parameters that correspond to human sneezing, we corroborate that the range of elasticities, velocities, and length scales seen in normal human sneezing can sometimes generate powerful atomizing sprays capable of propagating aerosols, as observed by Scharfman *et al.*[5] Moreover, the aerosolizing ability of a human sneeze is dependent on the elasticity of the saliva, which was found to vary by as much as an order of magnitude among the different donors, revealing that individuals with diminished saliva elasticities and high sneeze velocities are more likely to propagate droplets and aerosols.

2 Materials and methods

2.1 Materials

2.1.1 Human saliva samples. Due to the inability of reconstituted mucins to capture the rheological properties of native saliva,[18,19,36] human saliva samples were used in this study to conduct the impinging jet experiments. Five anonymous, healthy participants with no known allergies between the ages of 20 and 30 were selected to provide the saliva samples. The participants were instructed to brush their teeth 30 minutes prior to saliva collection. Saliva was collected in 50 mL plastic centrifuge tubes for a maximum period of two hours. Participants were not allowed to eat or drink fluids, except for water, during the collection period. To avoid degradation, the saliva samples were used for experiments within two hours after collection. Saliva samples were labeled using the letters A, B, C, D, and E. This study, including the collection, experimentation, and data management protocol, was approved by the ETH Zürich Ethics Commission as proposal 2021-N-111.

Other studies that use human saliva include an additional centrifugation step in their protocol.[19,36] We found that centrifuging the saliva for 30 minutes at 2700 rcf did not change the results from the impinging jet experiments when compared to the uncentrifuged samples. Thus, uncentrifuged samples were used in all experiments.

The density of the saliva was assumed to be equal to that of water.[5] The surface tension of the saliva samples was measured using a Wilhelmy balance and plate and their viscosity was determined using a standard rotational rheometer as outlined in Section 2.2.2. Data on the surface tension and viscosity measurements is available in Fig. S1 and S2 (ESI†). The values obtained for the viscosity and surface tension are in agreement with those previously reported in the literature.[45,46]

2.2 Methods

2.2.1 Impinging jet setup. An impinging jet setup is constructed as shown in Fig. 1, where each numbered item corresponds to a particular component as described below.

The saliva working fluid is poured inside two 50 mL Luer-Lok plastic syringes (Fisher Scientific BD Plastipak Syringe),
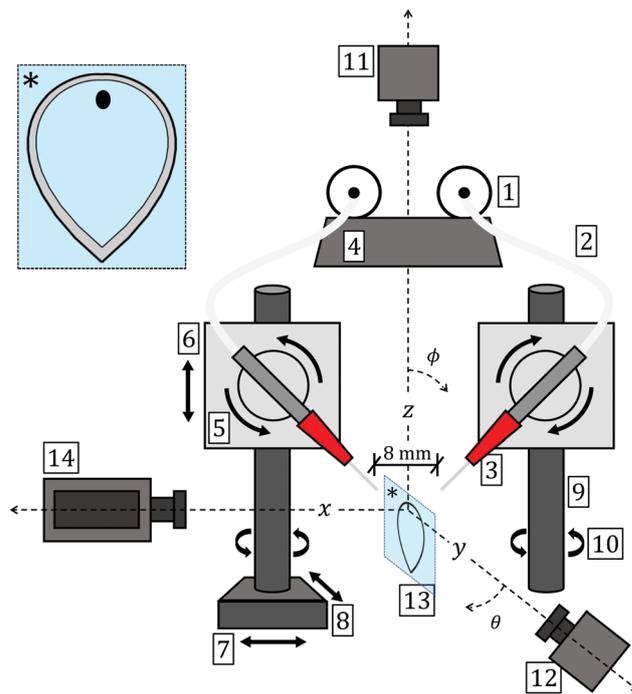

Fig. 1 Schematic of the impinging jet setup. Syringes [1] deliver salivary fluid through flexible tubing [2] to a pair of injectors with mountable needle tips of variable diameter [3]. The jet flow rate is set by a syringe pump [4]. The jet position is set *via* rotation and translation stages mounted onto optical posts [5–10] and a pair of monochrome cameras [11,12]. Upon impingement, the jets form a thin fluid sheet [13] that is recorded by a high speed camera [14]. The fluid sheet, marked by an asterisk, is reproduced in greater detail in the top left corner. The sheet is bounded by a cylindrical rim (shown in grey). The black ellipse marks the jet impingement location.

[1] which are connected to the impinging jet injectors *via* Teflon tubing [2]. The injectors, which lie on the x–z plane, consist of an aluminum core and a detachable stainless steel tip of variable diameter (Nordson EFD General Purpose Tips) [3]. Thus, the radius of the fluid jet, R, can be varied by switching out the needle tip. Tips with inner radii R of 0.125, 0.165, 0.205, and 0.255 mm are used in the present manuscript. It is assumed that the inner diameter of the tip is equal to the diameter of the fluid jet, and die swell is neglected.[47]

A double syringe pump (Harvard Apparatus PHD Ultra) [4] is used to pump the fluid into the impinging jets at the desired flow rate. Thus, by modulating the pump flow rate and needle radius, the jet velocity U and jet flow rate $Q = \pi R^2 U$ can be independently varied. Values of Q range between 0.2 and 1.75 mL s^{-1}, and values of U range between 0.98 and 14.3 m s^{-1} (depending on the prescribed flow rate and needle radius).

Each injector is connected to a rotation stage (Thorlabs Compact Rotation Stage XRNR1) [5], which is used to align the jets in the ϕ-plane. The impact angle 2ϕ of the jets is kept constant at $\pi/2$, such that the angle between each jet and the z-axis is $\pi/4$. Furthermore, the leftmost injector is also coupled to three linear translation stages (Thorlabs Travel Linear Translation Stage, XR25P/M) [6–8] that allow for precise alignment of the jets along the three Cartesian coordinate directions (*i.e.* the

vertical z-axis and the horizontal x- and y-axes). The injectors are mounted onto optical posts (Thorlabs RS300/M) [9], which are themselves mounted onto rotation stages (Thorlabs Compact Rotation Stage XRNR1) [10] that allow for jet alignment along the θ-axis. A pair of monochrome CMOS cameras (Thorlabs 1.6 MP Monochrome CMOS Camera CS165MU/M) [11–12] are mounted along the z- and y-axes and are used to aid in the visual alignment of the components, using the ThorCam camera software and ImageJ. The horizontal y-axis camera is used to align the jets in the ϕ, x, and z directions, while the vertical z-axis camera is used to align the jets in the θ and y directions. The jet impacting distance (along the x-axis) is set constant at 8 mm, measured via the y-axis camera.

Once the mountable tips are in place and alignment is complete, the pump flow rate is set and the experiment is allowed to begin. Upon impact of the two jets, a radially expanding sheet is formed in the y–z plane, perpendicular to the plane of the jets [13]. The sheet, marked by an asterisk, is reproduced in greater detail at the top left corner of Fig. 1. The sheet is bounded by a thicker cylindrical rim, shaded in grey. The small black ellipse near the top of the sheet marks the jet impingement location.

Movies of the sheet stability dynamics are recorded by a high-speed video camera (Photron Limited Fastcam Mini UX100) [14]. All videos are recorded at 6,400 fps with a shutter speed of 1/12 500 s^{-1}. Pixel-to-mm calibration of the resulting images is achieved by measuring the pixel width of a 1.83 mm outer diameter needle tip. A custom-made LED light source supplied by a 12 V DC current was fabricated to illuminate the fluid sheet. The light source is placed on top of the high-speed camera, and the videos are recorded against a white background.

2.2.2 Shear rheology. A standard rotational rheometer (Anton Paar MCR 302) with a double-gap Couette geometry was used for all viscosity and small amplitude oscillation measurements.

For all oscillatory measurements, a pre-shear step was conducted at a frequency ω of 1 Hz and strains γ between 0.5 and 10%, within the linear viscoelastic regime. Following the pre-shear step, a strain sweep was conducted at ω = 1 Hz and $0.5 \leq \gamma \leq 120\%$. To check for consistency, a frequency sweep within the linear regime (γ = 1% and $0.016 \leq \omega \leq 16$ Hz) was subsequently performed. Following the frequency sweep, a second strain sweep (ω = 1 Hz and $0.5 \leq \gamma \leq 120\%$) was conducted and the values of the elastic (G') and viscous (G'') moduli were compared among both strain sweeps. Experiments with comparable moduli values were kept, and all others were discarded.

Viscosity measurements were conducted at strain rates ($\dot{\gamma}$) between 10^{-1} and 10^4 s^{-1}. Each data point was measured for an amount of time greater than $1/\dot{\gamma}$ to ensure steady state is achieved. To determine the infinite shear viscosity μ_∞, the viscosity data was fit to a Sisko model, where the stress τ is given by

$$\tau = K\dot{\gamma}^n + \mu_\infty \dot{\gamma}, \tag{1}$$

and where K, n, and μ_∞ are adjustable parameters.

2.2.3 Extensional rheology. Extensional rheology measurements were performed using a Capillary Breakup Extensional Rheometer (Thermo Electron Corporation HAAKE CaBER 1) with 4 mm diameter circular endplates. The saliva was either directly introduced between the endplates or pre-sheared in order to mimic the conditions after exiting the needle tips in the impinging jet experiments. Pre-shearing was conducted by introducing the saliva inside a plastic Luer-Lok syringe and flowing it through a 0.165 mm inner radius needle tip at a velocity of 0.3 mL s^{-1} using a standard syringe pump.

The plates were initially separated by a vertical distance of 2 mm. Approximately 100 μL of saliva were injected between the circular plates using a 1 mL pipette in order to form a cylindrical bridge. A step strain was used to separate the plates from their initial distance to a final distance of 10 mm, reaching their final separation in 50 ms using a linear stretch profile. The evolution of the midplane diameter of the filament was recorded using a laser micrometer at a sampling rate of 3000 Hz.

In order to obtain a value for the polymer relaxation time, the midplane diameter $D_m(t)$ was plotted as a function of time t on a log-linear plot. The elastocapillary regime was identified as the straight-line region in the plot (see Fig. S3, ESI†), and the longest relaxation time λ of the polymer was obtained by determining the slope of the elastocapillary regime on the log-linear plot according to the following equation,

$$\frac{D_m(t)}{D_0} = \left(\frac{GD_0}{4\sigma}\right)^{1/3} \exp\left(-\frac{t}{3\lambda}\right), \tag{2}$$

where D_0 is the initial diameter of the thread, G is the elastic modulus, and σ is the interfacial tension.[22,23]

3 Results

3.1 Breakup of saliva sheets

3.1.1 Calculation of dimensionless parameter ranges. Human saliva samples were collected from five different anonymous donors (under approval by the ETH Zürich Ethics Commission as proposal 2021-N-111) and their physical properties were measured as explained in Section 2.1.1. Following sample collection, impinging jet experiments were conducted by varying the pump flow rate, $Q = \pi R^2 U$, and the jet radius, R, as outlined in Section 2.2.1.

The range of flow rates and jet radii are selected in order to encompass the range of dimensionless numbers encountered during human sneezing. The Reynolds, Weber, and Deborah numbers that characterize the sheet and rim dynamics in our impinging jet setup are given by:[24,25,32]

$$\text{Re} = \frac{\text{inertial driving force}}{\text{viscous driving force}} = \frac{\rho RU}{\mu_\infty}, \tag{3}$$

$$\text{We} = \frac{\text{inertial driving force}}{\text{capillary restoring force}} = \frac{\rho U^2 R}{\sigma_0}, \tag{4}$$

$$\mathrm{De} = \frac{\text{elastic time scale}}{\text{capillary time scale}} = \frac{\lambda}{\sqrt{\rho R^3 / \sigma_0}}. \tag{5}$$

The choice of material properties and geometrical scales is motivated by a physical analysis of the sheet geometry and the governing forces that drive fluid flow. The fluid density ρ is taken to be that of water.[5] σ_0 is the initial surface tension immediately upon contact of saliva and air; since mucin adsorption onto the air–saliva interface is a time-dependent process, the initial value for the surface tension is selected because sheet formation occurs almost immediately upon the contact of air and saliva. μ_∞ is the high frequency limit of the dynamic shear viscosity of the saliva. Although saliva is shear thinning,[15,18,21] μ_∞ is selected as the characteristic viscosity because the saliva samples experience elevated shear rates as they flow through the impinging jet nozzles and the viscosity thins. λ is the longest relaxation time of a polymer within the relaxation spectrum and, as such, sets the timescale for macromolecular unraveling of the entire mucin chain.[22,48] Table 1 presents a summary of the material properties of each saliva sample. Full data on the time and shear rate dependency of σ and μ, respectively, can be accessed in Fig. S1 and S2 (ESI†). The full relaxation time data is shown in Fig. 3(c).

The choice of U as the characteristic velocity for the sheet is justified in terms of results obtained for Newtonian sheets, where the velocity everywhere along the sheet remains constant and equal to the jet velocity U.[24–26] The jet radius R is selected as the characteristic length scale for the rim radius and sheet thickness, since the radius of the sheet's rim (and subsequently the sheet's thickness) scales as the jet radius R and is independent of U.[24]

We note that the dimensionless We and De can alternatively be expressed in terms of the relevant timescales that control the rim dynamics,

$$t_{\mathrm{cap}} = \sqrt{\frac{\rho R^3}{\sigma_0}}, \quad t_{\mathrm{proc}} = \frac{L}{U} = \frac{\rho U R^2}{\sigma_0}, \quad t_{\mathrm{elas}} = \lambda, \tag{6}$$

where the length L of the sheet scales as We R, as shown by Bremond and Villermaux.[24] t_{cap} is the capillary destabilization time that drives the Rayleigh–Plateau rim instability.[24] The process or convective timescale, t_{proc}, is the residence time of a material element flowing from the top to the bottom of the rim. t_{proc} is also equivalent to the reciprocal of the stretching rate experienced by a fluid element inside the rim. t_{elas} is the

polymer relaxation time, which sets the timescale for polymer unraveling. We note that We $= (t_{\mathrm{proc}}/t_{\mathrm{cap}})^2$ and De $= t_{\mathrm{elas}}/t_{\mathrm{cap}}$, as formulated in eqn (4) and (5).

It is imperative that the range of dimensionless numbers examined in the impinging jet experiments encompass those encountered during normal human sneeze events. Care must be taken to properly compare both phenomena, as the mechanism of sheet formation differs between real sneeze events and the impinging jet platform. In the jet configuration, steady-state sheet formation and flattening occur due to the inertia of the incoming fluid streams.[24,25] The momentum transferred by the two oblique impinging jets results in the formation of a flat sheet, in which fluid flows radially outwards from the impingement location.[24,25] The radial extent of the sheet is primarily set by a balance between the fluid inertia and surface tension, as reflected by We.[24,25]

In real sneeze events, the expelled saliva volume expands and flattens into a sheet due to the action of the aerodynamic pressure differential between the air moving with the sheet and the quiescent surroundings.[5,14,27,28] Thus, the size of a sneeze sheet is set by a balance between the aerodynamic inertial driving force and the surface tension restoring force, as reflected by the sneeze Weber number, We$_s$:

$$\mathrm{We}_s = \frac{\rho_{\mathrm{air}} U^2 L}{\sigma_0}, \tag{7}$$

where ρ_{air} is the density of air, U is the velocity of the sheet relative to the stagnant surroundings, L is the size of the sheet (where the total saliva volume is proportional to L^3), and σ_0 is the initial surface tension at the saliva/air interface.

Capillary instabilities are responsible for the destabilization of the rim in both the impinging jet platform and in real sneeze events. The sneeze Deborah number, De$_s$, represents the ratio of stabilizing elastic effects and destabilizing capillary effects,

$$\mathrm{De}_s = \frac{\lambda}{\sqrt{\rho R^3 / \sigma_0}}, \tag{8}$$

where λ is the saliva's relaxation time and R is the rim radius.

Since the viscosity, surface tension, and density of the saliva do not vary much among individuals, parameter values for the calculation of We$_s$ and De$_s$ are selected by setting constant values of $\sigma_0 = 50$ mN m^{-1} and $\rho_{\mathrm{air}} = 1$ kg m^{-3}, and allowing λ, U, L, and R to vary within a physiologically relevant range. A range of $2 \le \lambda \le 76$ ms is taken from the set of relaxation times in our data of pre-sheared saliva and from ref. 5, 20, 46 and 49.

Table 1 Physical properties of saliva

Saliva sample	Density, ρ (kg m^{-3})	Infinite shear viscosity, μ_∞ (mPa s)	Initial surface tension, σ_0 (mN m^{-1})	Pre-sheared relaxation time, λ (ms)
A	1000	1.64 ± 0.61^a	53.7 ± 2.2^a	$4.2\ (3.4–4.8)^b$
B	1000	1.43 ± 0.18^a	48.8 ± 0.4^a	$7.6\ (4.0–8.2)^b$
C	1000	1.70 ± 0.46^a	52.2 ± 3.3^a	$22.0\ (14.4–51.2)^b$
D	1000	2.44 ± 0.80^a	52.5 ± 1.4^a	$31.3\ (21.1–47.7)^b$
E	1000	2.22 ± 0.72^a	50.5 ± 5.9^a	$55.1\ (32.8–78.9)^b$

^{a} Data corresponds to the mean and standard deviation for three independent measurements per donor. ^{b} The median pre-sheared relaxation time is shown, where the data in parenthesis corresponds to the quartile 1 (Q1) and quartile 3 (Q3) values.

Table 2 Dimensionless numbers for human expiratory events and impinging jet setup

	Sneezing	Impinging jets
Re	—	1.1×10^2–1.5×10^3
We	5.0×10^0–7.4×10^2	4.6×10^0–7.5×10^2
De	1.3×10^0–1.9×10^2	7.6×10^0–2.8×10^2

Characteristic velocities and length scales are directly taken from ref. 5, 39, 40 and 50, which provide data for human sneezing. We take U to be the average sneezing velocity, where $5 \leq U \leq 35$ m s^{-1}. Sheet sizes formed during sneeze events fall within the range $1 \leq L \leq 3$ cm. R is taken to be the radius of the salivary filaments produced during sneezing, where $0.2 \leq R \leq 0.5$ mm, since the radius of the ligaments that are formed scales as the radius of the cylindrical rim.[24] The calculated range of We_s and De_s is presented in Table 2.

The range of jet radii and flow rates in our experiments is selected to match the range of dimensionless Weber and Deborah numbers encountered in human sneezing events. As mentioned in Section 2.2.1, jet tips with inner radii $R = 0.125$, 0.165, 0.205, and 0.255 mm are used for all experiments. The jet flow rate varies within the range $0.2 \leq Q \leq 1.75$ mL s^{-1} (which corresponds to jet velocities of $0.98 \leq U \leq 14.3$ m s^{-1}). The resulting range of Re, We, and De for the impinging jet setup is presented in Table 2.

3.1.2 Impinging jet experiments. Upon impact of the two saliva liquid jets, a radially expanding sheet is formed in the plane perpendicular to the plane of the jets. This radially expanding sheet is bounded by a thicker cylindrical rim which, at high inertia, can destabilize and fragment into ligaments and droplets.[24,25] Thus, for a given R, different flow and stability regimes are observed as the flow rate is increased.

Fig. 2 presents images of salivary sheets from donors A, C, and E, obtained using a constant $R = 0.205$ mm and varying Q. Saliva samples are labeled in terms of increasing resistance to breakup, where the sheets of saliva A are the least stable and break up into atomizing spray patterns at lower flow rates, and the sheets of saliva E are the most stable. Images of saliva samples B and D are provided in Fig. S4 (ESI†).

As the flow rate is increased, different sheet morphologies are sampled as the salivary sheet destabilizes. Four different stability regimes are identified, labeled as SR, WR, LI, and AS in Fig. 2. At low flow rates, a stable sheet with smooth rims (smooth rims – SR) is observed. As the flow rate is increased, the
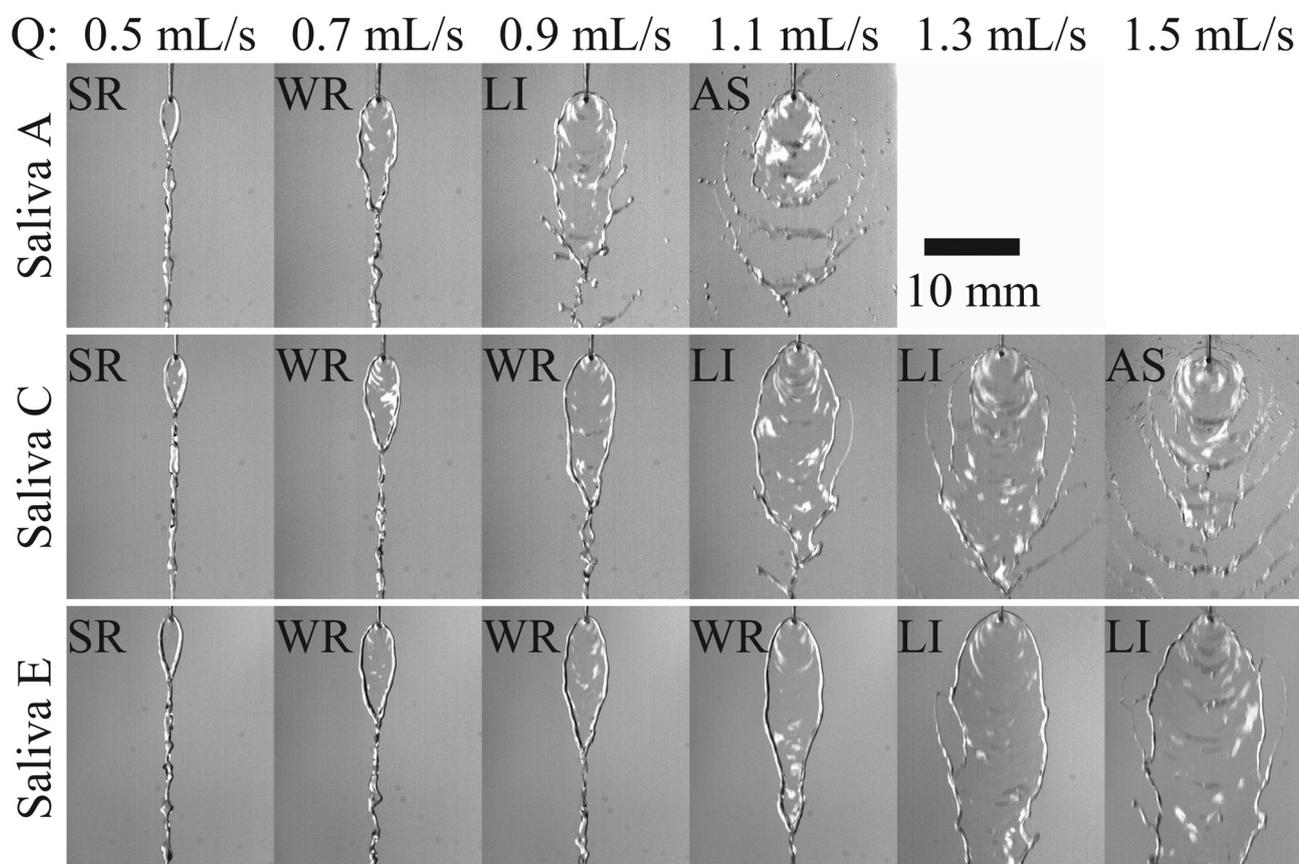

Fig. 2 High speed imaging of salivary sheets provided by donors A, C, and E in an impinging jet experiment, showing regimes of stability and breakup. Each row corresponds to an individual donor's saliva and columns represent the jet flow rate Q, where Q = 0.5, 0.7, 0.9, 1.1, 1.3, and 1.5 mL s^{-1}. A constant needle radius $R = 0.205$ mm is used for all experiments. Four regimes are used to classify the sheet's stability behavior: SR (smooth rims), WR (wobbly rims), LI (ligament formation), and AS (aerosolized spray). Regime transitions among the different donors occur at different flow rates.

sheet's rim begins to fluctuate and wobble (wobbly rims – WR), but the sheet structure remains intact. As inertia further increases, the rim fragments and ligaments that emanate from the rim are formed (ligament formation – LI). As the ligaments detach, they may subsequently break up into droplets. Finally, at the highest flow rates, the sheet disintegrates violently into a spray of droplets, culminating in full aerosolization of the salivary sheet (aerosolized spray – AS).

A stability analysis conducted for Newtonian solutions concluded that Rayleigh–Plateau capillary instabilities on the sheet's rim are responsible for ligament formation, and ligaments detach as oscillatory disturbances in the rim grow.[24,25] This mode of instability is also seen in our viscoelastic saliva solutions (see Fig. 2, saliva A, $Q = 0.9$ mL s^{-1}).

A second mode of instability is also observed, where the rim fragments and becomes discontinuous, and the downstream portion of the rim is ejected from the sheet as inertia deviates its path from its curved trajectory (see Fig. 2, saliva C, $Q = 1.3$ mL s^{-1}). We believe that this may correspond to a centrifugally forced Rayleigh–Taylor instability, since the liquid flowing along the rim is subject to an acceleration due to the rim's curvature.[24,51] For Newtonian solutions, the Rayleigh–Plateau instability is favored over the Rayleigh–Taylor phenomenon;[24] however, since ligament formation is also resisted by elasticity, it is hypothesized that a Rayleigh–Taylor destabilization process may also emerge alongside the traditionally seen capillary instability scenario if fluid elasticity is taken into account. Additional images documenting both observed ligament formation processes are presented in Fig. S5 and S6 (ESI†); further consideration of the stability analysis of elastic sheets is left to a possible future study.

Although the progression of the instability is the same for all donors (*i.e.* the four morphologies SR, WR, LI, and AS are sampled as Q increases and the sheets destabilize), the flow rates at which the transitions between the regimes occur is different. Thus, quantitative differences among individual donors are observed in terms of the flow rates at which the transitions from sheets to ligaments (WR → LI) and ligaments to sprays (LI → AS) occur, where saliva A has the lowest transition flow rates, saliva B has the second lowest transition flow rates, and so on.

For Newtonian sheets, the geometry, position, and stability of the rim is primarily set by the competition between surface tension and inertia.[24,25] However, capillary effects are not responsible for the differences in the WR → LI and LI → AS destabilization flow rates of the individual donors, since the surface tension of all saliva samples differs by less than 10%. The viscosity of the samples changes by at most a factor of two, so viscous effects are also not responsible for the differences in sheet fragmentation.

As shown in previous works on synthetic polymer solutions, enhanced elasticity stabilizes fluid sheets, forcing the system's inertia to reach higher magnitudes before the rim fragments into ligaments and droplets.[5,6,34] The same effect is seen in saliva solutions, where increases in salivary elasticity, mainly attributed to changes in the molecular weight, type, and/or

concentration of polymeric mucins,[49] are responsible for the delay in breakup among salivas A through E.

3.2 Rheological characterization of salivary fluids

We quantify the effect of elasticity *via* small amplitude oscillatory shear (SAOS) and extensional rheology CaBER experiments, as described in Sections. 2.2.2 and 2.2.3. A summary of the main results is presented in Fig. 3, and additional data on the oscillatory amplitude sweeps and the extensional capillary thinning experiments can be found in Fig. S3 and S7 (ESI†).

The linear elastic modulus (G'), linear viscous modulus (G''), and crossover strain (γ_c) for saliva samples A–E are depicted in panels (a) and (b) of Fig. 3. All saliva samples exhibit solid-like behavior at low strains within the linear viscoelastic regime, characteristic of a network-like structure of the mucin polymer at rest, with average values of G' between 0.2 and 0.8 Pa, in agreement with other studies.[18,21] However, linear viscoelastic properties do not correlate well with the stability and breakup behavior of the salivary sheets as prescribed in Fig. 2, where the naming of salivas A–E is assigned in order of increasing stability and a decreased susceptibility for aerosolization. This is not surprising, as the stability and breakup behavior of the salivary sheets corresponds to strong nonlinear deformations.

The onset of nonlinearity was also examined in order to assess whether there exists a correlation between the crossover strain and the saliva's resistance to breakup, as the onset of nonlinear behavior is associated with the breakdown of the fluid's network structure.[52,53] However, although the three most stable salivas (C, D, and E) have the largest γ_c magnitudes, there is – at best – a scant correlation between γ_c and salivary sheet stability.

Thus, we turn our focus to strongly nonlinear conditions, realized here by capillary thinning extensional rheology CaBER measurements, where large deformations and a strong extensional flow better interrogate the mucin polymer's response under extensional stresses, which dominate over shear stresses within salivary sheets.[9,24,25,31,32] An extensional flow field is also established within the rim of the impinging jet experiments, where a fluid element accelerates from zero velocity to the sheet's velocity as it travels from the top to the bottom of the sheet.[24]

CaBER experiments are used to obtain the saliva's characteristic relaxation time λ, which corresponds to the relaxation of the entire polymer chain following nonlinear deformations.[9,22,48] Fig. 3(c) depicts the results for the relaxation times of all saliva samples, where the saliva is either measured directly after collection or pre-sheared to mimic the conditions at the exit of the impinging jet nozzles, as described in Section 2.2.3. Previous studies report salivary extensional relaxation times between 1 and 10^2 ms, in agreement with our pre-sheared data.[20,49]

By comparing Fig. 2 and 3, it is evident that the relaxation times obtained from the extensional flow experiments now correlate well with the relative stability of the saliva samples, although the λ values for the pre-sheared saliva are smaller than those of the native samples by about an order of magnitude, revealing that the salivas undergo a structural
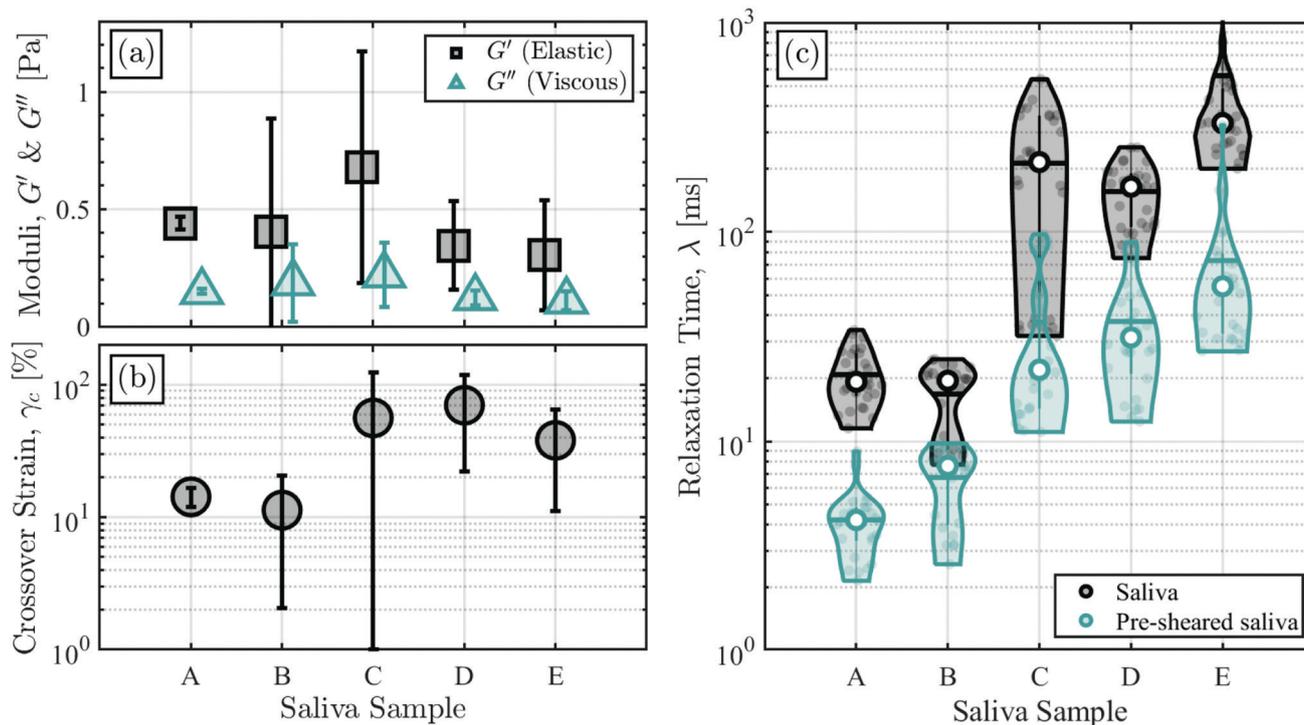
Fig. 3 Small amplitude oscillatory shear (SAOS) and filament stretching extensional rheology (CaBER) experiments are performed to measure the elasticity of the saliva samples from different donors. Shear rheology measurements of (a) the elastic (G') and viscous (G'') moduli and (b) the crossover strain (γ_c) cannot recapitulate the differences in sheet breakup and stability seen among salivas A–E. Each panel depicts the mean and standard deviation of three independent measurements conducted at a frequency of 1 Hz, using three different saliva samples for each donor. (c) Extensional rheology measurements of the relaxation time of saliva and pre-sheared saliva correlate well with the relative stability of salivas A–E as determined in the impinging jet experiments. The violin plots show data for 30 independent measurements conducted using three different saliva samples for each donor (10 measurements per sample). The median of all measurements is labeled by the white circle, and the mean is depicted by the bold horizontal line.

degradation due to the high shear rates they experience within the narrow impinging jet nozzles. In all subsequent analysis, the median relaxation time for the pre-sheared saliva (shown by the white circles in Fig. 3(c)), hereafter referred to as λ, will be used as the prime measure to quantify fluid elasticity during sheet breakup and atomization.

Although G' is used to quantify the effects of elasticity on sheet breakup in other studies,[34] it is evident that extensional rheology measurements of the solution's relaxation time are a better measure of the fluid's elasticity in relation to impinging jet experiments because of the breakdown of the quiescent network structure and the extensional nature of the flow field.[22,54] Furthermore, although salivary mucins exist in a dilute configuration, an order of magnitude analysis reveals that within the fluid sheets, they are elongated beyond the coil-stretch transition and extended sufficiently such that physical entanglements can occur[22] (see ESI† for order of magnitude analysis). Thus, CaBER measurements that involve large, nonlinear deformations that significantly stretch the individual polymers and allow for their physical overlap are better able to capture the state of the mucin molecules under flow when compared to SAOS experiments.

3.3 State diagrams for stability and aerosolizing ability

3.3.1 State diagrams for individual donors. State diagrams that depict the progression through all four stability regimes

are presented in Fig. 4 for the individual salivas A, C, and E as a function of We, Re, and De. State diagrams for salivas B and D and for a Newtonian 40% glycerol–water solution can be found in Fig. S8 (ESI†). Since We, Re, and De all have a different dependency on R and U, different regions of the phase space can be explored as the needle tip radius R and the pump flow rate Q are independently varied.

Several conclusions can be drawn from Fig. 4. Firstly, the range of Re where regime transitions occur does not change much among the individual donors; thus, we conclude that Re has a second-order effect on the stability of salivary sheets. To leading order, viscous effects do not play a role in shaping the morphology, dynamics, and stability of salivary liquid sheets. Indeed, inertial and capillary forces both dominate over viscous forces, as evidenced by the fact that Re $\gg$ 1 and Oh $\equiv$ $\mu_\infty/\sqrt{\rho R \sigma_0} \ll 1$ (where the Ohnesorge number, Oh, reflects the ratio of viscous over capillary stresses). This agrees with previous results obtained for Newtonian solutions, where Bremond and Villermaux determined that rim fragmentation is governed by the quantity $\sqrt{We}$, which reflects the ratio of the residence time of a fluid element to the capillary destabilization time.[24]

Most of the differences between the saliva samples is captured in the De vs. We phase space. Panels (d)–(f) reveal that the most elastic salivas (i.e. those with a larger De)
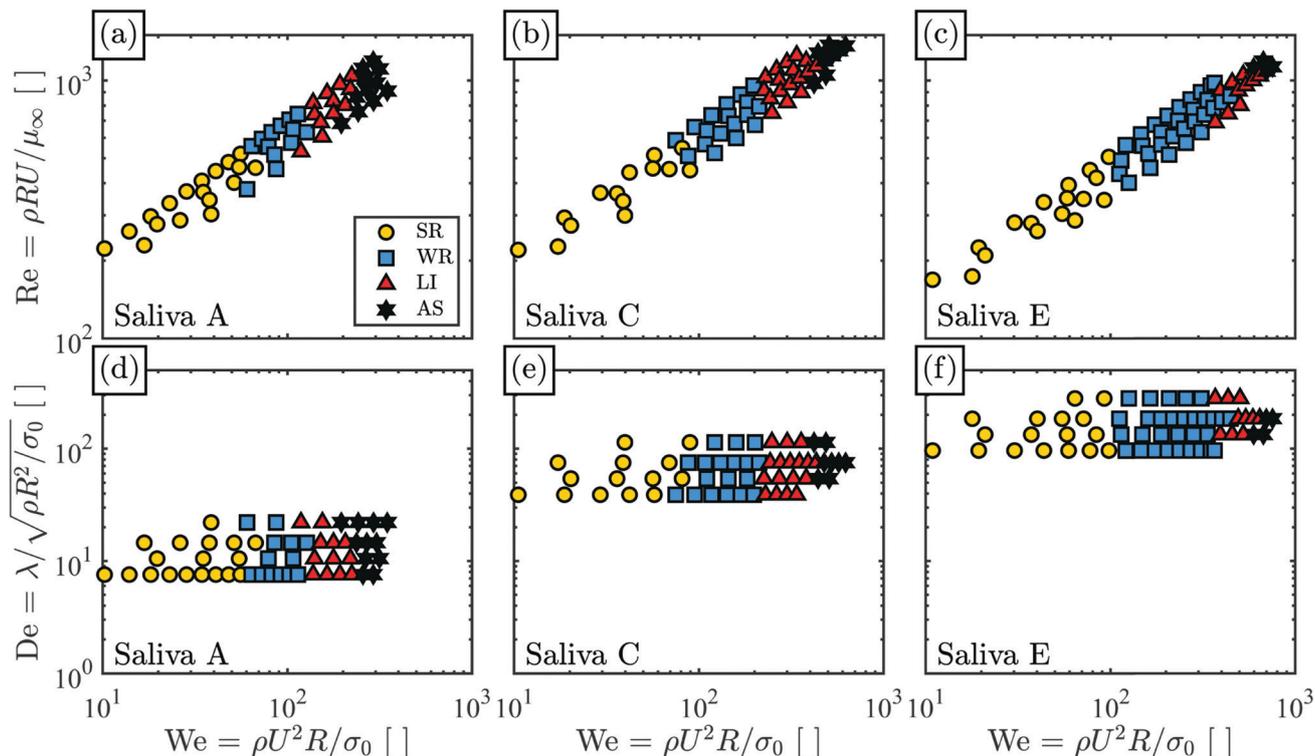
Fig. 4 State diagrams for the saliva of donors A, C, and E are constructed by varying three dimensionless groups: Re, We, and De. Panels (a)–(c) depict the Re vs. We phase space and panels (d)–(f) show the De vs. We phase space. Each colored marker corresponds to an individual impinging jet experiment conducted at a given Q and R. Four stability regimes are identified for the salivary sheet: smooth rims (SR), wobbly rims (WR), ligament formation (LI), and aerosolizing spray (AS).

experience sheet-to-ligament and ligament-to-spray transitions at higher values of We and De. Newtonian sheets begin to destabilize roughly when $t_{cap} < t_{proc}$, or when $\sqrt{We} \gtrsim 1$.[24] The presence of polymers is able to delay this transition: if the timescale associated with polymer unraveling is larger than the timescale for capillary destabilization ($t_{elas} > t_{cap}$), the polymer is more likely to resist the instability and maintain a persistent rim that does not break up into droplets. Thus, when elasticity is taken into account, the critical We for the sheet-to-ligament and ligament-to-droplet transitions to occur increases beyond its Newtonian value congruently with the solution's De. For Newtonian glycerol–water solutions, rim destabilization occurs at We as low as 25,[25,34] ‡ whereas for our viscoelastic saliva solutions, aerosolization occurs at We between 10^2 and 10^3.

Salivas that are more elastic, or those with a larger λ, require larger velocities (i.e. higher inertia) in order for aerosolization to occur. For example, as seen in Fig. 4(d), a person whose saliva has a similar relaxation time as saliva A (the least elastic saliva), is more prone to produce ligaments and/or aerosols upon activities such as sneezing. However, as seen in Fig. 4(f), a person whose saliva has a similar composition as saliva E (which has the highest λ) has a smaller propensity to generate aerosols. Thus, our results highlight the importance of salivary

‡ Note the differences in the definition of We in ref. 25 and 34 We has been recalculated according to our definition.

elasticity in deterring aerosol formation and emphasize the variability of this parameter among the different donors, where individuals with more elastic salivas are less prone to produce aerosols.

3.3.2 Universal state diagrams. We now wish to generalize these findings and combine the results of donors A–E to construct universal state diagrams applicable to any normal human saliva sample. These universal state diagrams can be represented in terms of De and We only, since it was shown that Re has a second order effect in determining the stability of salivary sheets.

Fig. 5(a) presents the universal salivary sheet stability state diagram, which combines all the data points from the impinging jet experiments of the five donors A–E. The De vs. We phase space encompassed by each of the four stability regimes is identified as a shaded colored region within the dotted lines, which are drawn to guide the eye. In addition, the ranges of De_s and We_s associated with normal human sneezing (as derived in Section 3.1.1) are depicted by the cross-hatch shaded region.

Our results support the fact that human sneezing is capable of generating ligaments and aerosols fully outside the respiratory tract, as evidenced by Scharfman et al.[5] This result validates the use of our impinging jet setup as a platform to systematically study human sneezing. The generation of such ligaments and aerosols is strongly influenced by the variable saliva viscoelasticity among individuals. Since the saliva donors
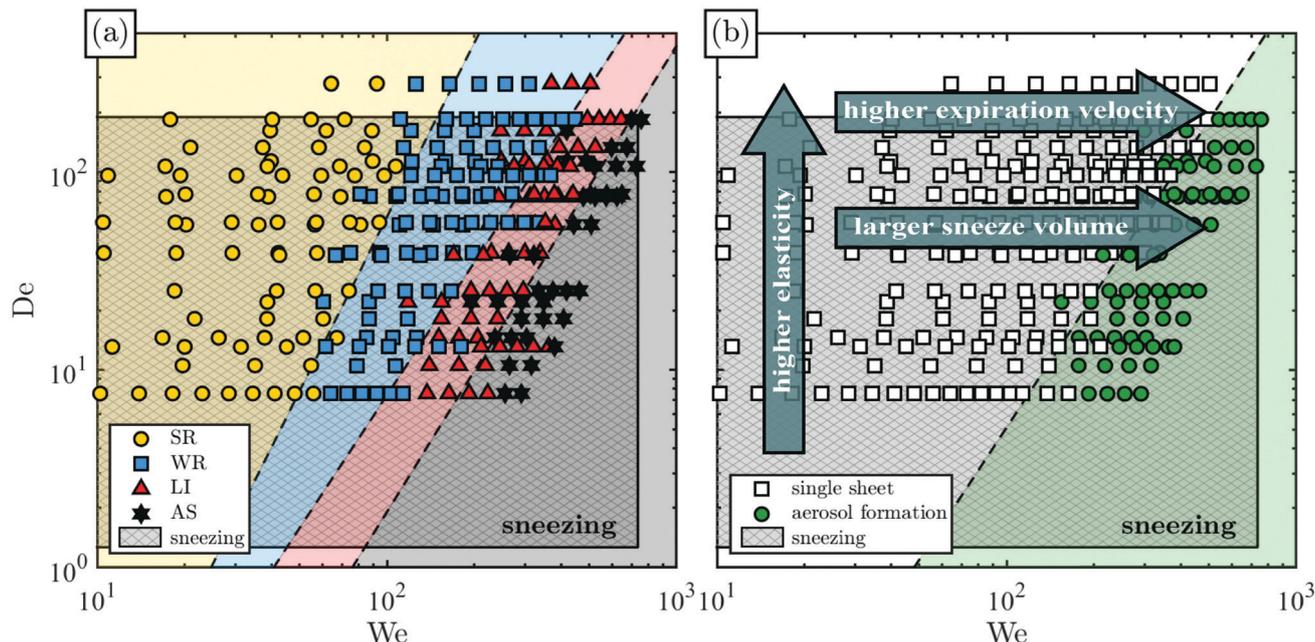
Fig. 5 Universal state diagrams in terms of De and We are constructed using the impinging jet data from all donors A–E. Markers correspond to individual impinging jet experiments, and the De vs. We phase space encompassed by each regime is depicted by the shaded color regions within the dotted lines. Dimensionless parameter ranges for normal human sneezing are marked by the cross-hatch shaded regions. (a) The salivary sheet stability state diagram identifies regions corresponding to the four sheet stability regimes: smooth rims (SR), wobbly rims (WR), ligament formation (LI), and aerosolizing spray (AS). (b) The salivary sheet aerosolization state diagram identifies regions of aerosol formation, based on whether the saliva remains bound as a continuous volume (single sheet) or breaks up into droplets (aerosol formation). Arrows depict movements along the phase space as the saliva elasticity, volume, and expiration velocity are independently increased.

in our study were all healthy individuals between the ages of 20 and 30, we can expect an even broader variation in saliva viscoelasticity among the global population.

Furthermore, our results also highlight the importance of this variable saliva viscoelasticity for other aerosol-generating human expiratory events, such as speaking, singing, or coughing. As documented by Abkarian et al., during human speech salivary sheets are generated at the edge of the lips, which stretch and break the saliva films into ligaments and droplets.[6] Thus, although some aspects of the kinematics of the flows studied in our impinging jet experiments (i.e. two-dimensional freely suspended and radially expanding sheets) differ from those encountered during human speech (i.e. two-dimensional expanding sheets with constrained boundaries), our experiments suggest that elasticity and variations thereof should play an important role in determining the stability and onset of breakup of salivary sheets and ligaments produced during processes such as speaking, singing, or coughing.

The De vs. We universal stability state diagram has predictive capabilities, as the stability properties of any human saliva sample with a known relaxation time can be extracted as a function of the sneeze velocity, sneeze volume, and salivary ligament thickness, assuming that these parameters fall within the specified normal physiological range.

Furthermore, the effects of changing salivary elasticity, expelled saliva volume, and/or sneeze velocity can be more directly assessed. For instance, to elucidate the effects of

increasing saliva elasticity, we consider a scenario where U, L, and R are kept constant and λ is allowed to increase. As λ increases we move vertically upwards along the De axis, traversing the phase space AS → LI → WR → SR where stable sheets form at the highest λ and aerosolizing sprays at the lowest λ. Similarly, if the sneeze velocity increases and all other parameters remain constant, we move horizontally from left to right, traversing regions SR → WR → LI → AS and moving from stable sheets at the lowest U to aerosolizing sprays at the highest U. The characteristic sheet size L, which is proportional to the expelled saliva volume, obeys the same trends as U. Thus, it is evident from Fig. 5(a) that as saliva elasticity decreases, the expelled saliva volume increases, and/or the sneeze expiration velocity increases, ligaments and sprays are more likely to form upon sneezing.

Although the universal stability state diagram recapitulates the dominant physical forces at the rim and provides a convenient way to examine the sheet morphology and stability progression, it does not provide the most straightforward way of answering the more societally relevant question of whether or not a particular sneeze will produce aerosols. In order to answer this question in the most simple and unambiguous way, we construct a universal aerosolization state diagram, shown in Fig. 5(b).

Here, we propose a binary phase classification based on whether or not droplets that detach from the sheet are produced. In other words, we classify each experiment based on

whether the salivary fluid remains bound as a continuous volume (single sheet in Fig. 5(b)) or breaks up into individual droplets (aerosol formation in Fig. 5(b)). Thus, while all sheets with smooth rims (SR) or wobbly rims (WR) remain intact as single sheets and all aerosolizing sprays (AS) aerosolize by definition, ligament formation (LI) may or may not be accompanied by droplet detachment. At lower inertia, ligaments remain bound to the sheets at all times (single sheet); as inertia increases, the beads-on-a-string instability develops and the ligaments destabilize into droplets that detach and escape the sheet volume (aerosol formation).

The universal aerosolization diagram is a practical takeaway of this study, and can be used without the need to rigorously understand the physical nature of sheet breakup and rim destabilization. It unambiguously shows that individuals with diminished saliva elasticity, larger expelled saliva volumes, and high sneeze velocities are more likely to propagate droplets and aerosols upon sneezing, and can be easily used to assess the aerosolization propensity of any human saliva sample with known elasticity.

4 Discussion

Aside from the documented variations in salivary viscoelasticity among individuals, there can also be variations in the mechanical properties of a single individual's saliva. These variations can occur as a function of age, diet, and/or activity.[16,49,55] For instance, extensional rheology measurements of human saliva show that its elasticity is strongly correlated with an individual's age. This effect is caused by age-related physiological changes that reduce the salivary water content and increase its total protein concentration.[49]

The same study also showed that stimulated saliva production – through activities such as chewing or consuming acidic foods – leads to an increase in the salivas's elasticity by approximately 20% when compared to unstimulated saliva.[49] Specifically, stimulated saliva taken directly from the submandibular/sublingual region of the mouth (the main production site of salivary mucins) has a relaxation time of about 400 ms, an order of magnitude higher than that of unstimulated saliva taken from the same region.[49,55] Thus, under stimulation, the submandibular/sublingual glands produce a higher percentage of mucins and glycoproteins, which increase the saliva's elasticity and hence decrease its aerosolization ability. Thus, if only elasticity were to be taken into account, it would be advisable for individuals to engage in activities that shift their saliva production from an unstimulated to a stimulated mode, such as chewing gum. However, stimulated saliva flow rates are an order of magnitude higher than those of unstimulated saliva, which could lead to an overall increase in the total aerosol content despite its higher elasticity.[16,55]

Aside from the interplay between mucus elasticity and flow rate, there is also a complex cooperation between disease-spreading pathogens and mucus composition. For example, mucins can modulate the virulence of certain bacteria by altering the expression of genes that control bacterial colonization and pathogenicity.[56] Pathogens can also influence mucus composition in order to enhance their mobility and create an optimal environment for reproduction.[57] For instance, the growth of bacterial biofilms that promote antibiotic resistance is enhanced by the creation of thick, dehydrated mucus.[58] The enhanced elasticity of dehydrated mucus lowers its aerosolization ability, which would act to reduce the spread of pathogens; however, a higher elasticity simultaneously increases their survival and infectiousness, as aerosols are not transported as efficiently out of the bronchial tract by the cilia lining its walls.

A number of works also suggest that variations in human speech patterns, such as language, pronunciation, and speech volume, can also play a role in determining the aerosolization propensity of a given individual's saliva. A recent study by Abkarian and Stone documents that the pronunciation of plosives (such as the letters 'p' or 'b') induces the emission of a larger number of droplets when compared to other sounds.[6] A separate study by Asadi *et al.* reports that the concentration of emitted aerosols increases with speech loudness.[59] They also note that there are certain individuals, termed "speech super-emitters", who produce up to an order of magnitude more droplets than the average person. This phenomenon cannot be explained by speech patterns alone, and thus the authors hypothesize that physiological factors must be at play. It is possible that superemitters, who produce a significantly elevated number of droplets, feature a combination of low saliva elasticities, loud speaking volumes (*i.e.* high speech velocities), and high rates of plosive pronunciation.

Thus, the study of the mechanical properties of mucus in relation to the spreading of contagious diseases is a complicated, multifaceted problem that relies on a deep understanding of the multiple factors that affect mucus elasticity, mucus production rates, pathogen virulence, and human speech patterns. Our study advances this understanding by quantifying the effects of salivary mucus elasticity and other dynamic conditions on aerosolization and elucidating the extent to which variations in elasticity among individuals can account for disparities in aerosol production.

5 Conclusions

An impinging jet setup systematically replicates the breakup and aerosolization behavior observed during human expiratory events occurring outside of the respiratory tract, where the expelled saliva flattens into a sheet that can destabilize into ligaments and droplets with the details of breakup being caused by an interplay of inertia, capillarity, and elasticity. We tested human saliva samples provided by five different anonymous donors, highlighting quantitative differences in their elasticity that directly influence the onset of ligament and aerosol formation. This asserts the importance of taking fluid elasticity into account when studying aerosolization processes with human saliva.

The balance of inertial, capillary, viscous, and elastic forces within the salivary sheets is expressed in terms of the

dimensionless Weber, Deborah, and Reynolds numbers, which were used to construct phase diagrams that portray our experimental results and recapitulate the stability and aerosolizing ability of all saliva samples. Typical human sneezing events are mapped onto the state diagrams, allowing for a direct comparison between our impinging jet experiments and normal physiological behavior. We corroborate the fact that sneezing events can induce aerosolization processes fully outside of the human body, where the propensity of aerosolization increases in a manner proportional to the sneeze ejection velocity and ejected saliva volume and inversely proportional to the saliva's elasticity.

Our results also highlight the general importance of salivary elasticity in deterring ligament breakup and aerosol generation, which has ramifications for other aerosol-producing human expiratory activities such as speaking, singing, or coughing. Thus, we show that inherent variations in the composition of an individual's saliva have a direct influence in the generation of droplets and aerosols, which can help explain differences in disease transmission among the human population.

Author contributions

M. R. H. and J. V. designed research (conceptualization, methodology); M. R. H. and L. R. performed research (investigation); M. R. H. analyzed data (formal analysis); M. R. H. and J. V. wrote the manuscript (M. R. H. – writing original draft; M. R. H. and J. V. – writing review & editing); J. V. provided research supervision, resources, and funding acquisition.

Conflicts of interest

The authors declare no competing interests.

Acknowledgements

Notes and references

1 Transmission of SARS-CoV-2: implications for infection prevention precautions, 2020.

2 L. Bourouiba, E. Dehandschoewercker and J. W. M. Bush, *J. Fluid Mech.*, 2014, **745**, 537–563.

3 Y. Cheng, N. Ma, C. Witt, S. Rapp, P. S. Wild, M. O. Andreae, U. Pöschl and H. Su, *Science*, 2021, **372**, 1439–1443.

4 W. C. K. Poon, A. T. Brown, S. O. L. Direito, D. J. M. Hodgson, L. Le Nagard, A. Lips, C. E. MacPhee,

D. Marenduzzo, J. R. Royer, A. F. Silva, J. H. J. Thijssen and S. Titmuss, *Soft Matter*, 2020, **16**, 8310–8324.

5 B. Scharfman, A. Techet, J. Bush and L. Bourouiba, *Exp. Fluids*, 2016, **57**, 1–9.

6 M. Abkarian and H. A. Stone, *Phys. Rev. Fluids*, 2020, **5**, 102301.

7 G. S. Settles, *Annu. Rev. Fluid Mech.*, 2006, **38**, 87–110.

8 C. C. Wang, K. A. Prather, J. Sznitman, J. L. Jimenez, S. S. Lakdawala, Z. Tufekci and L. C. Marr, *Science*, 2021, **373**, eabd9149.

9 L. Bourouiba, *Annu. Rev. Biomed. Eng.*, 2021, **23**, 547–577.

10 R. Mittal, R. Ni and J.-H. Seo, *J. Fluid Mech.*, 2020, **894**, F2.

11 G. Johnson, L. Morawska, Z. Ristovski, M. Hargreaves, K. Mengersen, C. Chao, M. Wan, Y. Li, X. Xie, D. Katoshevski and S. Corbett, *J. Aerosol Sci.*, 2011, **42**, 839–851.

12 M. Jain, R. S. Prakash, G. Tomar and R. V. Ravikrishna, *Proc. R. Soc. A*, 2015, **471**, 20140930.

13 M. A. Kohanski, L. J. Lo and M. S. Waring, *Int. Forum Allergy Rhinol.*, 2020, **10**, 1173–1179.

14 M. Pilch and C. A. Erdman, *Int. J. Multiphase Flow*, 1987, **13**, 741–757.

15 A. Sarkar, F. Xu and S. Lee, *Adv. Colloid Interface Sci.*, 2019, **273**, 102034.

16 G. H. Carpenter, *Annu. Rev. Food Sci. Technol.*, 2013, **4**, 267–276.

17 S. Takehara, M. Yanagishita, K. A. Podyma-Inoue and Y. Kawaguchi, *PLoS One*, 2013, **8**, 1–9.

18 O. W. Meldrum, G. E. Yakubov, M. R. Bonilla, O. Deshmukh, M. A. McGuckin and M. J. Gidley, *Sci. Rep.*, 2018, **8**, 1–16.

19 B. D. E. Raynal, T. E. Hardingham, J. K. Sheehan and D. J. Thornton, *J. Biol. Chem.*, 2003, **278**, 28703–28710.

20 S. J. Haward, J. A. Odell and M. Berry, *Rheol. Acta*, 2011, **50**, 869–879.

21 W. H. Schwarz, *J. Dent. Res.*, 1987, **66**, 660–666.

22 C. Clasen, J. P. Plog, W.-M. Kulicke, M. Owens, C. Macosko, L. E. Scriven, M. Verani and G. H. McKinley, *J. Rheol.*, 2006, **50**, 849–881.

23 S. Sur and J. Rothstein, *J. Rheol.*, 2018, **62**, 1245–1259.

24 N. Bremond and E. Villermaux, *J. Fluid Mech.*, 2006, **549**, 273–306.

25 J. W. M. Bush and A. E. Hasha, *J. Fluid Mech.*, 2004, **511**, 285–310.

26 D. Hasson and R. E. Peck, *AIChE J.*, 1964, **10**, 752–754.

27 E. Reyssat, F. Chevy, A.-L. Biance, L. Petitjean and D. Quéré, *EPL*, 2007, **80**, 34005.

28 E. Villermaux and B. Bossa, *Nat. Phys.*, 2009, **5**, 697–702.

29 C. Clasen, P. M. Phillips, L. Palangetic and J. Vermant, *AIChE J.*, 2012, **58**, 3242–3255.

30 X. Chen, D. Ma, V. Yang and S. Popinet, *Atomization Sprays*, 2013, **23**, 1079–1101.

31 V. M. Entov, A. N. Rozhkov, U. F. Feizkhanov and A. L. Yarin, *Mech. Tech. Phys.*, 1986, **27**, 41.

32 A. L. Yarin, *Free liquid jets and films: hydrodynamics and rheology*, Longman Group UK Limited, London, 1993.

33 B. Keshavarz, E. C. Houze, J. R. Moore, M. R. Koerner and G. H. McKinley, *Phys. Rev. Lett.*, 2016, **117**, 154502.

34 S. Jung, S. D. Hoath, G. D. Martin and I. M. Hutchings, *J. Non-Newtonian Fluid Mech.*, 2011, **166**, 297–306.

35 E. Miller, B. Gibson, E. McWilliams and J. P. Rothstein, *Appl. Phys. Lett.*, 2005, **87**, 014101.

36 B. D. E. Raynal, T. E. Hardingham, D. J. Thornton and J. K. Sheehan, *Biochem. J.*, 2002, **362**, 289–296.

37 R. Hamed, D. M. Schenck and J. Fiegel, *Soft Matter*, 2020, **16**, 7823–7834.

38 A. M. Hasan, C. F. Lange and M. L. King, *J. Non-Newtonian Fluid Mech.*, 2010, **165**, 1431–1441.

39 C. Chao, M. Wan, L. Morawska, G. Johnson, Z. Ristovski, M. Hargreaves, K. Mengersen, S. Corbett, Y. Li, X. Xie and D. Katoshevski, *J. Aerosol Sci.*, 2009, **40**, 122–133.

40 J. W. Tang, A. D. Nicolle, C. A. Klettner, J. Pantelic, L. Wang, A. B. Suhaimi, A. Y. L. Tan, G. W. X. Ong, R. Su, C. Sekhar, D. D. W. Cheong and K. W. Tham, *PLoS One*, 2013, **8**, 1–7.

41 Y. Zhang, G. Feng, Y. Bi, Y. Cai, Z. Zhang and G. Cao, *Sustainable Cities and Society*, 2019, **51**, 101721.

42 G. Busco, S. R. Yang, J. Seo and Y. A. Hassan, *Phys. Fluids*, 2020, **32**, 073309.

43 M. E. Rosti, S. Olivieri, M. Cavaiola, A. Seminara and A. Mazzino, *Sci. Rep.*, 2020, **10**, 22426.

44 Mariam, A. Magar, M. Joshi, P. S. Rajagopal, A. Khan, M. M. Rao and B. K. Sapra, *ACS Omega*, 2021, **6**(26), 16876–16889.

45 R. G. Schipper, E. Silletti and M. H. Vingerhoeds, *Arch. Oral Biol.*, 2007, **52**, 1114–1135.

46 J. R. Stokes and G. A. Davies, *Biorheology*, 2007, **44**, 141–160.

47 H. A. Barnes, J. F. Hutton and K. Walters, *An introduction to rheology*, Elsevier Science Publishers B.V., Netherlands, 1989.

48 M. Rubinstein and R. H. Colby, *Polymer physics*, Oxford University Press, United Kingdom, 2003.

49 E. Zussman, A. L. Yarin and R. M. Nagler, *J. Dent. Res.*, 2007, **86**, 281–285.

50 M. Abkarian, S. Mendez, N. Xue, F. Yang and H. A. Stone, *Proc. Natl. Acad. Sci. U. S. A.*, 2020, **117**, 25237–25245.

51 M. M. Scase and R. J. A. Hill, *J. Fluid Mech.*, 2018, **852**, 543–577.

52 T. G. Mezger, *Applied rheology: with Joe Flow on rheology road*, Anton Paar, 2018.

53 J. W. Goodwin and R. W. Hughes, *Rheology for chemists – an introduction*, The Royal Society of Chemistry, Cambridge, United Kingdom, 2000.

54 R. G. Larson, *J. Rheol.*, 2005, **49**, 1–70.

55 S. P. Humphrey and R. T. Williamson, *J. Prosthet. Dent.*, 2001, **85**, 162–169.

56 J.-F. Sicard, G. Le Bihan, P. Vogeleer, M. Jacques and J. Harel, *Front. Cell. Infect. Microbiol.*, 2017, **7**, 387.

57 J. P. Celli, B. S. Turner, N. H. Afdhal, S. Keates, I. Ghiran, C. P. Kelly, R. H. Ewoldt, G. H. McKinley, P. So, S. Erramilli and R. Bansil, *Proc. Natl. Acad. Sci. U. S. A.*, 2009, **106**, 14321–14326.

58 S. Moreau-Marquis, B. A. Stanton and G. A. O'Toole, *Pulm. Pharmacol. Ther.*, 2008, **21**, 595–599.

59 S. Asadi, A. S. Wexler, C. D. Cappa, S. Barreda, N. M. Bouvier and W. D. Ristenpart, *Sci. Rep.*, 2019, **9**, 2348.